GeSn Alloys with ~21% Sn Grown by Effusion Cell Molecular Beam Epitaxy

Diandian Zhang,[1] Nirosh M. Eldose,[2] Dinesh Baral,[1,2] Hryhorii Stanchu,[2] Mourad Benamara,[1] Wei Du,[1,2] Gregory J. Salamo,[2,3] and Shui-Qing Yu[1,2,a)]

[1] Department of Electrical Engineering and Computer Science, University of Arkansas, Fayetteville, Arkansas, 72701, USA
[2] Institute for Nanoscience and Engineering, University of Arkansas, Fayetteville, Arkansas, 72701, USA
[3] Department of Physics, University of Arkansas, Fayetteville, Arkansas, 72701, USA

[a)] Electronic mail: syu@uark.edu

We report the epitaxial growth of high quality GeSn alloys with Sn compositions up to 21.25 ±1% using effusion-cell molecular beam epitaxy (MBE). Achieving such a high Sn content with effusion cells is particularly significant, since these sources typically impose stronger radiative heating on the substrate which is a factor long considered a major obstacle to high-Sn GeSn epitaxy. Contrary to the prevailing assumption that high growth rates are good for suppressing Sn segregation, we demonstrate that carefully controlled low fluxes, combined with stable ultra-low substrate temperatures, enable significant Sn incorporation even under effusion-cell conditions. Structural analyses by High resolution X-ray diffraction (HR-XRD), reciprocal space mapping (RSM), atomic force microscopy (AFM), and transmission electron microscopy (TEM) confirm sharp interfaces, high crystallinity, and smooth surfaces at high Sn contents. These findings establish the feasibility of MBE-grown high-Sn GeSn even under diffusion cells, thereby broadening opportunities for Si-compatible photonic and quantum devices.

I. INTRODUCTION

The realization of efficient light emission from Si-compatible materials remains a central challenge in silicon photonics[1-4]. GeSn alloys have emerged as a promising candidate, as incorporating Sn into Ge results direct-bandgap emission at sufficiently high Sn compositions[5-10]. For example, using chemical vapor deposition (CVD) direct-bandgap GeSn material and corresponding GeSn laser and detectors have been reported[5, 11-14]. However, despite its advantages in ultra-high vacuum operation, precise flux control, and compatibility with complex heterostructures, MBE has struggled to incorporate enough Sn to realize even direct-bandgap GeSn, let alone high-performance devices[15, 16]. The challenge of achieving sufficient Sn content GeSn can potentially be due to low growth rate and growth temperatures, lattice mismatch between substrate and film, and lack of temperature control resulting from heating by the effusion cells, which together have resulted in significantly lower Sn content GeSn when compared to CVD growth[17, 18].

In this work, we revisited this challenge and demonstrate that MBE, when carried out under carefully stabilized substrate temperatures and low flux and temperature conditions, can reliably produce high quality GeSn layers with Sn contents at least has high as 21.25 ±1%, even when using diffusion cells. This work not only realizes the growth of high-Sn GeSn with effusion cell MBE but also offers a new perspective on MBE GeSn growth, emphasizing that maintaining a stable substrate temperature is key. Structural and morphological analyses further reveal the interplay between Sn incorporation, strain accommodation, and crystalline quality, offering new insights into the growth kinetics of metastable group-IV alloys. By extending the accessible Sn composition range in MBE, this work establishes MBE as a viable pathway toward

direct-bandgap GeSn and its integration into Si-based optoelectronic and quantum technologies with high quality interfaces.

II. EXPERIMENTAL

A. Material growth

In this work, high-Sn-content GeSn samples were grown on Ge substrates by MBE using effusion cells. Prior to growth, the substrates were cleaned in 2.5% HF and deionized water, and immediately loaded into the load-lock chamber. They were then transferred to the degassing chamber and baked at 350 °C for 2 h to remove residual moisture, followed by baking in the growth chamber at 750 °C for 1 h. The base pressure of the growth chamber was maintained below 3×10^{-11} Torr.

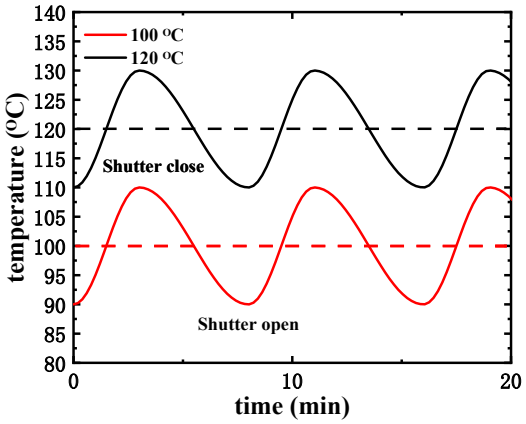

FIG.1. Schematic illustration of the temperature evolution during the growth process.

Before GeSn deposition, a Ge buffer layer was grown using the Ge effusion cell. Subsequently, GeSn layers were deposited at low temperature using Ge and Sn effusion cells with a growth rate of 0.35 nm/min. All samples were grown at 100 °C, except for sample S3, which was grown at 120 °C. During the growth process, substrate heating from thermal radiation was minimized by periodically opening and closing the cell shutters, and by employing small fluxes to reduce radiation from the effusion cells. The schematic diagram in Fig. 1 illustrates the temperature evolution during the growth process. Please note that this is a conceptual illustration rather than measured temperature data. The structural details of all samples are summarized in Table I, with the highest Sn content reaching 21.25% (± 1%).

TABLE I. The structural details of all GeSn samples

Samples	Substrates	T_{GeSn} **(°C)**	$T_{Ge\ cell}$ **(°C)**	$T_{Sn\ cell}$ **(°C)**	GeSn thickness **(nm)**	Intended Sn **(%)**	XRD Sn **(%)**	Strain **(%)**
S1	Ge (001)	100±10	1220	990	9	15	14.7	-2.1
S2		100±10		980	17	14	14	-2.0
S3		120±10		990	18	15	15	-2.1
S4		100±10		1010	45	18	18	-2.8
S5		100±10		1030	10	22	21.25 ±1%	-3.1

B. Characterization

HR-XRD and RSM were performed to obtain the lattice parameters, in-plane ($a_{//}$) and out-plane ($a_{\perp}$), of the GeSn layer. Using the following equation, the lattice constant can be quickly obtained.

$$a_{//} = 2\sqrt{2}/Q_x,\ a_{\perp} = 4/Q_y \quad (1)$$

Where Qx and Qy are the coordinates of (−2 −2 4) RSM. The lattice constant (a_0) and Sn content of GeSn can be obtained by solving the Vegard's law and the Poisson's relationship. The strain ($\varepsilon_{//}$) and relaxation degree (R) can be calculated by using the following equations:

$$\varepsilon_{//} = \frac{a_{//} - a_0}{a_0},\ R = \frac{a_{//} - a_{sub}}{a_0 - a_{sub}} \quad (2)$$

Where a_0 and a_{sub} are the lattice constants of GeSn and Ge substrate respectively.

Fig.2 shows the HR-XRD results of the samples along (004) direction. Clear Laue fringes can be observed for most of the samples, indicating a sharp interface of GeSn/Ge and a good crystal quality of GeSn layers. The Sn content shown on the rocking curves are 14.7%, 14%, 15%, 18%, and 21.25% (± 1%) for sample S1 to S5. It should be noted that, because the (004) curve of sample S5 is relatively weak and exhibits a large linewidth, a certain degree of uncertainty is introduced. Therefore, we include an error range of ±1% in the estimation of its Sn composition. Moreover, through simulation of the XRD rocking curves, the thicknesses of the samples were determined to be 9, 17, 18, 45, and 10 nm for S1 to S5, respectively. It is worth noting that, for MBE utilizing effusion cells, a Sn content of 21.25% (± 1%) is a remarkably high value[16, 19, 20].

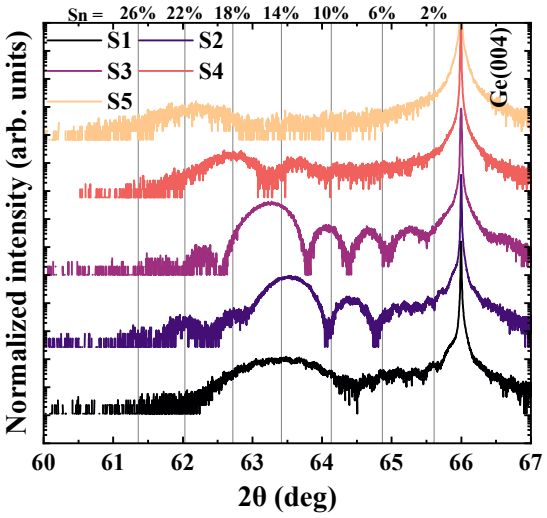

FIG. 2. High-resolution $2\theta - \omega$ curves of GeSn samples grown on Ge (100) substrate measured along (004) direction.

Comparing the XRD results, sample S3 exhibits pronounced Laue fringes and a significantly smaller FWHM than S1 and S2. In contrast, S1 shows a much larger FWHM without clear Laue fringes. Given its smaller thickness, the expected larger fringe period in S1 may account for the absence of observable fringes, making it difficult to directly assess its crystalline quality relative to S2. On the other hand, comparison between S2 and S3 reveals that S3 has a smaller FWHM. Since both samples have comparable thicknesses and Sn compositions, this indicates that S3 possesses higher crystalline quality, which can be attributed to its higher growth temperature.

In addition, samples S4 and S5 were also grown to investigate the growth of high-Sn-content GeSn. As shown in the figure, sample S4 exhibits a distinct GeSn peak along with well-defined Laue fringes, indicating relatively good crystalline quality. However, the crystalline quality shows some degradation compared with samples S2 and S3. This is expected, as the higher Sn composition inevitably introduces larger strain, which in turn

degrades the crystalline quality of the GeSn layer. Furthermore, in sample S5 with a high Sn composition of 21.25 ±1%, the GeSn peak becomes noticeably broad and shallow, which typically indicate degraded crystal quality and a rougher surface morphology. Given the greater mismatch induced by the higher Sn composition, it is expected that the crystal quality would be poorer compared to GeSn alloys with lower Sn compositions.

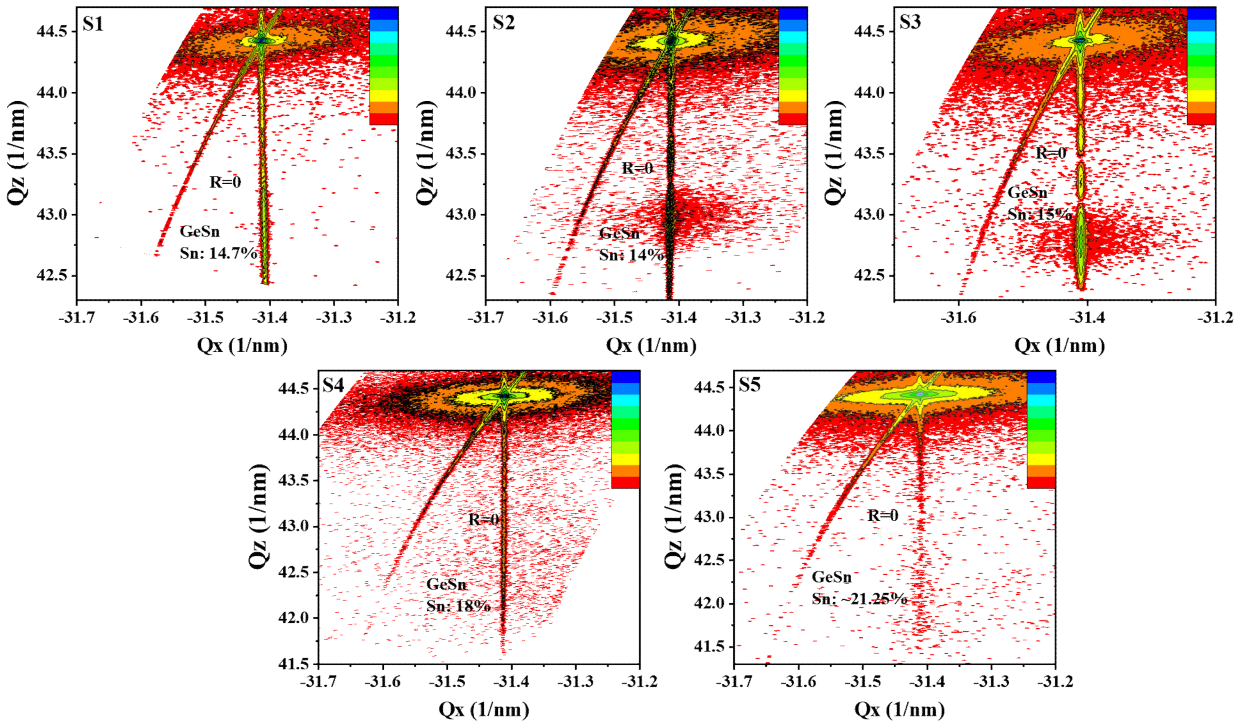

FIG. 3. RSM around the asymmetric (−2 −2 4) reflection of GeSn samples. The scale represents signal intensity, with a transition from red to blue indicating increasing intensity.

Fig. 3 shows the RSM around the asymmetric (-2 -2 4) reflection of the GeSn samples. It is clear that all the GeSn layers have a same horizontal coordinate (Q_x) as Ge substrate, indicating that the GeSn layers are fully strained compared to Ge substrate. The gradient-like peaks originate from the Laue fringes.

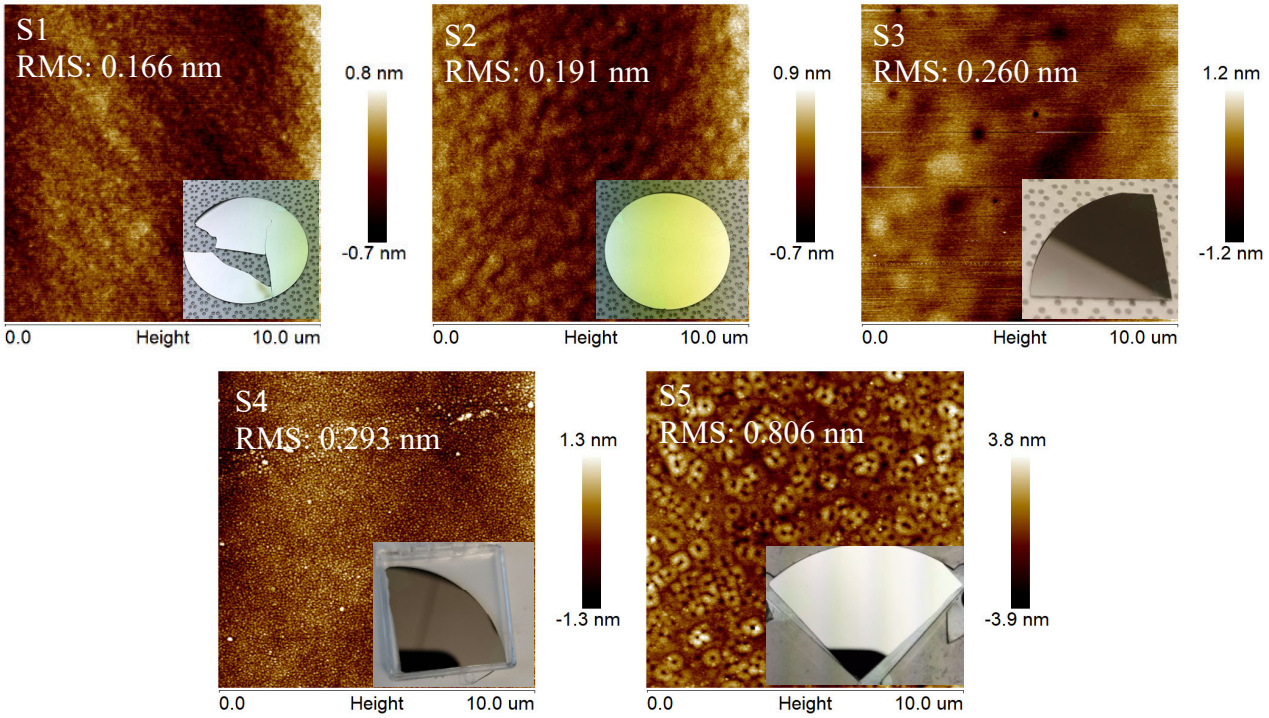

FIG .4. AFM images of the samples. Inserts are the optical pictures of the samples.

AFM was carried out to investigate the surface morphology of the samples. As shown in Fig. 4, all samples exhibit very smooth surfaces. This is primarily due to the limited surface diffusion of adatoms at low temperatures, which suppresses the formation of large three-dimensional islands and favors layer-by-layer (Frank–van der Merwe) growth of GeSn[21, 22]. In addition, low temperatures help inhibit phase separation or Sn clustering in GeSn alloys, leading to uniform composition and minimized surface roughness[23]. The relatively low thermal energy also reduces stress-driven surface roughening, resulting in a more planar morphology. Sample S1 to S4 exhibit very smooth surfaces with RSM of 0.16 to 0.29 nm. S1 and S2 show quite similar surface morphologies, since their growth conditions are nearly identical, with only a slight difference in thickness. Compared with S1 and S2, S3 has a smoother surface, despite exhibiting larger fluctuations. The effect of kinetic roughening is reduced at higher

growth temperatures; however, long-range surface undulations remain unavoidable. None of the samples exhibit Sn segregation**.** In contrast, a different surface morphology was observed in S5. A relatively rough, porous surface is displayed in the figure with an RMS roughness of 0.806 nm, which is much bigger than those in S1 to S4. We attribute this to the greater strain induced by the higher Sn composition. Under significant strain, the growth is more likely to transition to a three-dimensional mode, where the growing surface tends to exhibit larger fluctuations, resulting in a more wrinkled surface morphology. The inserts are optical pictures of each of the samples. All of the samples show a relatively flat and shiny surface without Sn segregation.

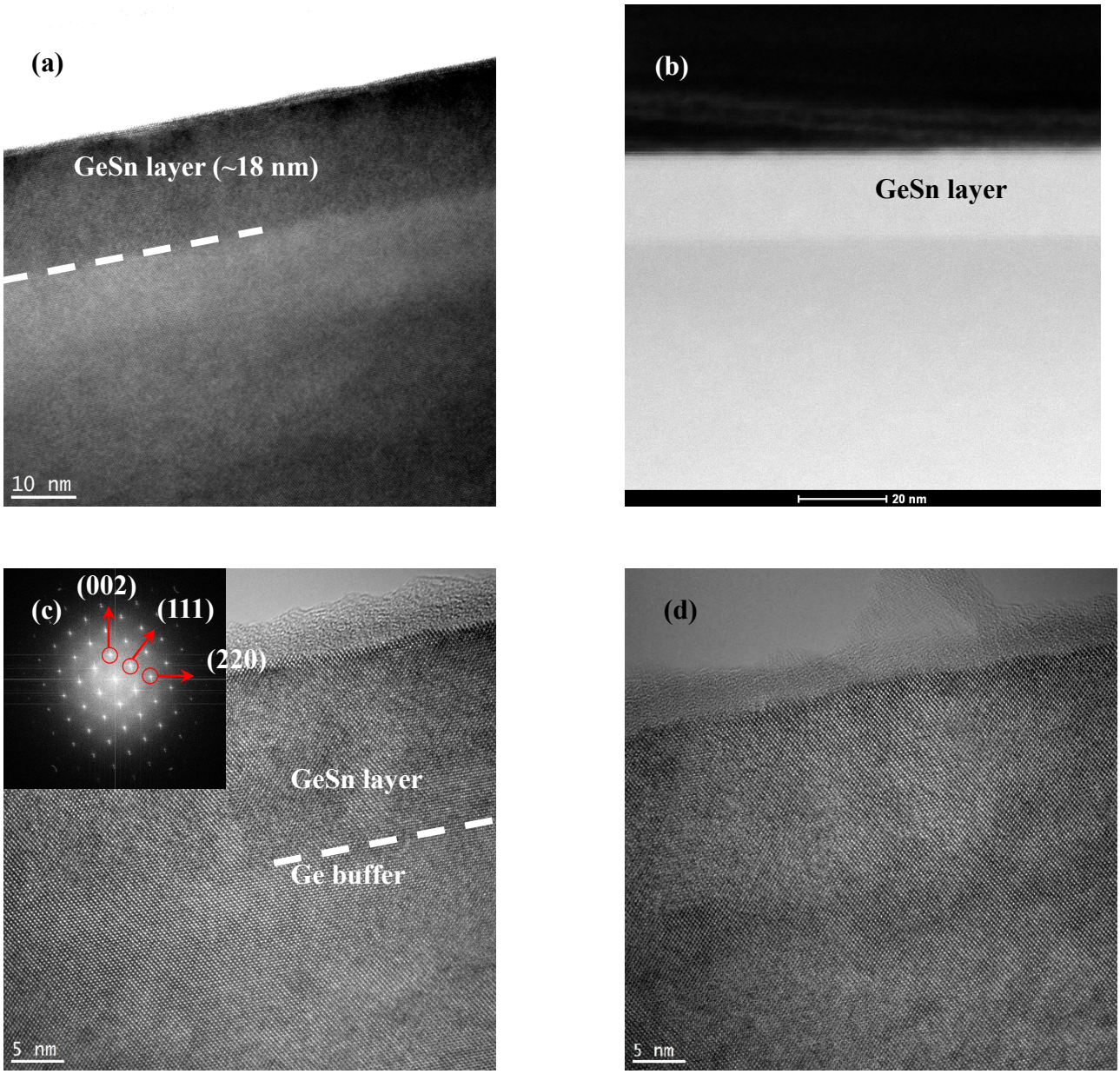

FIG .5. (a) bright field (BF) and (b) High-Angle Annular Dark-Field (HAADF) images of sample S3. (c) and (d) higher resolution (HR) TEM image near the GeSn/Ge interface, the insert in (c) is the FFT image.

To examine the quality of the samples in more detail Fig. 5 shows the TEM images of sample S3 as an example. As shown in Fig.5 (a), a clear GeSn/Ge interface can be observed. A ~18 nm GeSn layer is clear shown in the image without any defect. Fig. 5(b) presents the HAADF image. Consistent with previous observations, no defects are

observed, and the interfaces are distinctly flat and sharp. Fig. 5(c) and (d) show higher resolution TEM images at different locations near the GeSn/Ge interfaces, exhibiting a perfect single crystal structure, with no dislocations observed, confirming the excellent crystalline quality of the GeSn sample.

III. SUMMARY AND CONCLUSIONS

In this work, by carefully controlling the substrate temperature and minimizing radiation-induced temperature deviations, we prevent Sn atoms from gaining additional energy from thermal radiation, thereby keeping them in a “low-energy” state during growth. This effectively suppresses Sn segregation and enables the incorporation of Sn up to 21.25% ± 1% in GeSn using effusion-cell MBE, marking one of the highest Sn contents achieved by this technique. Our results indicate that temperature stability is highly beneficial for the growth of high-Sn GeSn, even under low flux conditions. Beyond setting a new benchmark for Sn content in MBE-grown GeSn, this study provides important insights into the growth mechanisms of metastable group-IV alloys. The demonstrated up to 21.25 ±1% Sn and the observed trade-off between crystalline quality and Sn composition highlight key design considerations for GeSn-based heterostructures. By effectively controlling the influence of thermal radiation, this work provides a new pathway for growing higher-Sn-content GeSn on Ge or Ge-buffered Si, and lays the foundation for the realization of Si-compatible light emitters, photodetectors, and quantum structures fabricated with the precision and versatility of MBE.

ACKNOWLEDGMENTS

This work was supported by the μ-ATOMS, an Energy Frontier Research Center funded by the U.S. Department of Energy, Office of Science, Basic Energy Sciences under award DE-SC0023412. This work was also supported in part by the Office of Naval Research (Grant No. N00014-24-1-2651)

AUTHOR DECLARATIONS

Conflicts of Interest

The authors have no conflicts to disclose.

DATA AVAILABILITY

The data that support the findings of this study are available from the corresponding authors upon reasonable request.

REFERENCES

1. Y. Han, H. Park, J. Bowers and K. M. Lau, Advances in Optics and Photonics **14** (3) (2022).
2. D. Thomson, A. Zilkie, J. E. Bowers, T. Komljenovic, G. T. Reed, L. Vivien, D. Marris-Morini, E. Cassan, L. Virot, J.-M. Fédéli, J.-M. Hartmann, J. H. Schmid, D.-X. Xu, F. Boeuf, P. O'Brien, G. Z. Mashanovich and M. Nedeljkovic, Journal of Optics **18** (7) (2016).
3. S. Q. Yu, G. Salamo, W. Du, B. Li, G. Sun, R. A. Soref, Y. H. Zhang and G. E. Chang, presented at the 2022 Device Research Conference (DRC), IEEE, Piscataway, NJ, 2022.
4. R. Soref, Silicon **2** (1), 1-6 (2010).
5. S. A. Ghetmiri, W. Du, J. Margetis, A. Mosleh, L. Cousar, B. R. Conley, L. Domulevicz, A. Nazzal, G. Sun, R. A. Soref, J. Tolle, B. Li, H. A. Naseem and S.-Q. Yu, Applied Physics Letters **105** (15), 151109 (2014).
6. O. Moutanabbir, S. Assali, X. Gong, E. O'Reilly, C. A. Broderick, B. Marzban, J. Witzens, W. Du, S. Q. Yu, A. Chelnokov, D. Buca and D. Nam, Applied Physics Letters **118**, 110502 (2021).

7. N. Rosson, S. Acharya, A. M. Fischer, B. Collier, A. Ali, A. Torabi, W. Du, S.-Q. Yu and R. C. Scott, Journal of Vacuum Science & Technology B **42** (5), 052210 (2024).
8. J. Zheng, Z. Liu, C. Xue, C. Li, Y. Zuo, B. Cheng and Q. Wang, Journal of Semiconductors **39** (6) (2018).
9. S. Wirths, D. Buca and S. Mantl, Progress in Crystal Growth and Characterization of Materials **62** (1), 1-39 (2016).
10. L. Jiang, J. D. Gallagher, C. L. Senaratne, T. Aoki, J. Mathews, J. Kouvetakis and J. Menéndez, Semiconductor Science and Technology **29**, 115028 (2014).
11. S. Acharya, H. Stanchu, R. Kumar, S. Ojo, M. Alher, M. Benamara, G. E. Chang, B. Li, W. Du and S. Q. Yu, IEEE Journal of Selected Topics in Quantum Electronics **31** (1: SiGeSn Infrared Photon. and Quantum Electronics), 1-7 (2025).
12. Y. Zhou, S. Ojo, C.-W. Wu, Y. Miao, H. Tran, J. M. Grant, G. Abernathy, S. Amoah, J. Bass, G. Salamo, W. Du, G.-E. Chang, J. Liu, J. Margetis, J. Tolle, Y.-H. Zhang, G. Sun, R. A. Soref, B. Li and S.-Q. Yu, Photonics Research **10** (1) (2021).
13. G. Abernathy, S. Ojo, A. Said, J. M. Grant, Y. Zhou, H. Stanchu, W. Du, B. Li and S. Q. Yu, Sci Rep **13** (1), 18515 (2023).
14. Y. Miao, G. Wang, Z. Kong, B. Xu, X. Zhao, X. Luo, H. Lin, Y. Dong, B. Lu, L. Dong, J. Zhou, J. Liu and H. H. Radamson, Nanomaterials (Basel) **11** (10) (2021).
15. F. Wan, C. Xu, X. Wang, G. Xu, B. Cheng and C. Xue, Journal of Crystal Growth **577** (2022).
16. L. Kormoš, M. Kratzer, K. Kostecki, M. Oehme, T. Šikola, E. Kasper, J. Schulze and C. Teichert, Surface and Interface Analysis **49** (4), 297-302 (2017).
17. Y. Liang, D. West and S. Zhang, Applied Physics Letters **126**, 202109 (2025).
18. F. Maia de Oliveira, N. M. Eldose, D. Baral, H. Stanchu, S. Kryvyi, D. Zhang, M. Zamani-Alavijeh, M. Benamara, Y. I. Mazur, W. Du, S.-Q. Yu and G. J. Salamo, Crystal Growth & Design **25** (15), 6023-6029 (2025).
19. D. Schwarz, H. S. Funk, M. Oehme and J. Schulze, Journal of Electronic Materials **49** (9), 5154-5160 (2020).
20. M. Oehme, K. Kostecki, M. Schmid, F. Oliveira, E. Kasper and J. Schulze, Thin Solid Films **557**, 169-172 (2014).
21. P. Politi, G. Grenet, A. Marty, A. Ponchet and J. Villain, Physics Reports **324** (5), 271-404 (2000).
22. D. J. Eaglesham, Journal of Applied Physics **77** (8), 3597-3617 (1995).
23. K. A. Bratland, Y. L. Foo, T. Spila, H. S. Seo, R. T. Haasch, P. Desjardins and J. E. Greene, Journal of Applied Physics **97**, 044904 (2005).